NeuroImage 147 (2017) 669–677

Contents lists available at ScienceDirect

NeuroImage

journal homepage: www.elsevier.com/locate/neuroimage

Full Length Articles

PETPVE12: an SPM toolbox for Partial Volume Effects correction in brain PET – Application to amyloid imaging with AV45-PET☆

Gabriel Gonzalez-Escamilla[a,*], Catharina Lange[b], Stefan Teipel[a,c], Ralph Buchert[b], Michel J. Grothe[a,c,**], for the Alzheimer's Disease Neuroimaging Initiative

[a] German Center for Neurodegenerative Diseases (DZNE) - Rostock/Greifswald, Rostock, Germany
[b] Department of Nuclear Medicine, Charité – Universitätsmedizin Berlin, Berlin, Germany
[c] Department of Psychosomatic Medicine, University of Rostock, Rostock, Germany

ARTICLE INFO

Keywords:
Alzheimer's disease
Amyloid imaging
PET
MRI
Partial Volume Effects correction

ABSTRACT

Positron emission tomography (PET) allows detecting molecular brain changes *in vivo*. However, the accuracy of PET is limited by partial volume effects (PVE) that affects quantitative analysis and visual interpretation of the images. Although PVE-correction methods have been shown to effectively increase the correspondence of the measured signal with the true regional tracer uptake, these procedures are still not commonly applied, neither in clinical nor in research settings. Here, we present an implementation of well validated PVE-correction procedures as a SPM toolbox, PETPVE12, for automated processing. We demonstrate its utility by a comprehensive analysis of the effects of PVE-correction on amyloid-sensitive AV45-PET data from 85 patients with Alzheimer's disease (AD) and 179 cognitively normal (CN) elderly. Effects of PVE-correction on global cortical standard uptake value ratios (SUVR) and the power of diagnostic group separation were assessed for the region-wise geometric transfer matrix method (PVEc-GTM), as well as for the 3-compartmental voxel-wise "Müller-Gärtner" method (PVEc-MG). Both PVE-correction methods resulted in decreased global cortical SUVRs in the low to middle range of SUVR values, and in increased global cortical SUVRs at the high values. As a consequence, average SUVR of the CN group was reduced, whereas average SUVR of the AD group was increased by PVE-correction. These effects were also reflected in increased accuracies of group discrimination after PVEc-GTM (AUC=0.86) and PVEc-MG (AUC=0.89) compared to standard non-corrected SUVR (AUC=0.84). Voxel-wise analyses of PVEc-MG corrected data also demonstrated improved detection of regionally increased AV45 SUVR values in AD patients. These findings complement the growing evidence for a beneficial effect of PVE-correction in quantitative analysis of amyloid-sensitive PET data. The novel PETPVE12 toolbox significantly facilitates the application of PVE-correction, particularly within SPM-based processing pipelines. This is expected to foster the use of PVE-correction in brain PET for more widespread use. The toolbox is freely available at http://www.fil.ion.ucl.ac.uk/spm/ext/#PETPVE12.

1. Introduction

Positron Emission Tomography (PET) imaging is a nuclear medicine imaging technique that enables the quantitative assessment of molecular brain processes *in vivo*. However, brain PET images are still difficult to interpret because of the limited spatial resolution of current generation PET scanners, which causes the image signal to suffer from partial volume effects (PVE), i.e. the measured signal at a given gray matter (GM) region reflects a mixture of the true regional signal with signal from surrounding brain tissue (Hoffman et al., 1979). The magnitude of this effect is particularly pronounced when the size of the measured GM region is small compared to the resolution of the reconstructed PET image (Hoffman et al., 1979). Hence, PVEs become more severe due to regional brain atrophy as occurring in advanced aging and neurodegenerative disease. For PET tracers characterized by relatively high GM signal compared to the surrounding tissue (e.g. 18F-fluorodeoxyglucose [FDG]), this can lead to substantial underestimation of the true GM activity, whereas overestimation of the GM signal is

☆ Data used in preparation of this article were obtained from the Alzheimer's Disease Neuroimaging Initiative (ADNI) database (adni.loni.usc.edu). As such, the investigators within the ADNI contributed to the design and implementation of ADNI and/or provided data but did not participate in analysis or writing of this report. A complete listing of ADNI investigators can be found at: ⟨http://adni.loni.usc.edu/wp-content/uploads/how_to_apply/ADNI_Acknowledgement_List.pdf⟩.

* Corresponding author.
** Correspondence to: Deutsches Zentrum für Neurodegenerative Erkrankungen e.V. (DZNE), Standort Rostock/Greifswald, Gehlsheimer Straße 20, D-18147 Rostock, Germany.
E-mail addresses: gabriellbk@gmail.com (G. Gonzalez-Escamilla), michel.grothe@dzne.de (M.J. Grothe).

http://dx.doi.org/10.1016/j.neuroimage.2016.12.077
Received 23 September 2016; Accepted 27 December 2016
Available online 28 December 2016
1053-8119/

to be expected in settings where the true tracer signal is relatively low compared to the signal in adjacent tissue (e.g. high unspecific white matter binding in amyloid-PET scans) (Matsubara et al., 2016; Schmidt et al., 2015). PVE correction (PVEc) is intended to account for the mixing of signals from different tissue types in the measured PET signal in order to provide a better approximation of the true regional tracer uptake.

Multiple PVEc algorithms have been proposed, some of which require only the PET image itself (reviewed in Erlandsson et al., 2012), whereas more robust methods make use of detailed anatomical information provided by a high-resolution MRI scan from the same subject to correct the estimated GM signal, either at the voxel level (Muller-Gartner et al., 1992) or for segmented brain regions (Rousset et al., 1998a).

PVEc methods have been shown to adequately model the mixing of signals from neighboring tissues and to increase the correspondence of the measured PET signal with the true regional tracer uptake (Erlandsson et al., 2012). However, PVEc methods also depend on a range of model assumptions that may not always hold true or may only be roughly approximated in the imaging data, resulting in PVEc-induced noise amplification (Erlandsson et al., 2012; Greve et al., 2016; Hogenauer et al., 2016; Thomas et al., 2011). Hence, the net effect of PVEc on the power of PET to detect disease-related changes is not always clear a priori which has limited its routine application (Soret et al., 2007). Furthermore, the net effect of PVEc on the diagnostic power of PET depends on the tracer as well as on the particular diagnostic context and study endpoint. Thus, whereas PVEc does not improve the diagnostic potential of FDG-PET for distinguishing between AD patients and healthy controls (Ibanez et al., 1998; Meltzer et al., 1996; Samuraki et al., 2007), it should be beneficial for a more accurate detection of AD-related cortical amyloid pathology with recently developed amyloid binding PET radiotracers, given that these typically suffer from high unspecific white matter binding and ensuing signal spill-in effects (Matsubara et al., 2016; Schmidt et al., 2015). However, for novel PET tracers such as these, there is relatively less information available regarding the effects of PVEc.

Apart from the concerns about the diagnostic fitness of PVEc-based analyses, a more pragmatic reason for the limited use of PVEc in PET, even in research settings, may be the lack of PVEc processing routines in most of the commonly used open-source software packages for medical image processing and analysis, such as SPM (http://www.fil.ion.ucl.ac.uk/spm/), FSL (http://fsl.fmrib.ox.ac.uk/fsl/fslwiki/FSL), or AFNI (http://afni.nimh.nih.gov/afni/). Thus, most researchers who wish to apply PVEc methods to their PET data are currently forced to use external software packages for this task, most notably the commercial software PMOD (PMOD Technologies Ltd., Adliswil, Switzerland) or a specialized free software package called PVElab (Quarantelli et al., 2004). While these packages are in the main compatible, the external PVEc routines do not seamlessly integrate into the processing workflows of current releases of the major open-source analysis suites.

The objective of the present work was to implement the best validated voxel- and region-based PVEc methods as an easy to use toolbox for the SPM software (Ashburner and Friston, 2000), one of the most widely used open-source software packages for PET image processing and analysis. Usage and utility of the methods provided by the toolbox is demonstrated in an analysis assessing the effects of PVEc on AV45-PET (Florbetapir F18) data. AV45-PET belongs to the family of novel F18-labeled amyloid binding radiotracers that are of critical importance in the field of Alzheimer's disease (AD) and neurodegenerative disease research (Clark et al., 2011; Villemagne et al., 2012). Although initial evidence for a beneficial effect of PVEc methods on tracer quantification in amyloid-sensitive PET data has been reported recently (Brendel et al., 2015; Matsubara et al., 2016; Rullmann et al., 2016; Su et al., 2016), PVEc is not yet commonly applied to amyloid-PET in clinical or research settings, presumably due to the logistic difficulties of implementing the methods in commercial software.

2. Methods

2.1. Correction of partial volume effects in PET images

Correction for PVE in PET images was implemented in the PETPVE12 toolbox using two well-established PVEc algorithms: the voxel-wise method as defined by Muller-Gartner et al. (1992) (PVEc-MG), as well as the region-based geometric transfer matrix method (PVEc-GTM) (Rousset et al., 1998a).

2.1.1. Voxel-based PVEc: background and implementation

The PVEc-MG method is a three compartment PVEc method, which extends simpler two compartmental approaches that only distinguish between brain parenchyma and surrounding CSF signal (Meltzer et al., 1996; Videen et al., 1988), and is currently one of the most widely used MRI-based methods for voxel-wise PVEc of PET images (Erlandsson et al., 2012). In brief, the method assumes that the observed PET signal in any given GM voxel is a spatial weighted average of the true tracer uptake signal in the GM voxel and the signal in surrounding white matter (WM) and cerebrospinal fluid (CSF), where the spatial weighting is determined by the point spread function (PSF) of the PET scanner. The proposed PVEc algorithm consists of correcting possible signal spill-in effects into the GM compartment, as well as signal spill-out into the surrounding tissue:

$$C_{PVEc-GM} = \frac{C_{obs} - C_{WM}(WM \oplus PSF) - C_{CSF}(CSF \oplus PSF)}{GM \oplus PSF}$$

where C_{obs} is the observed GM signal in the acquired PET scan; *GM*, *WM* and *CSF* are the respective tissue compartments, convolved by the scanner *PSF*; C_{WM} and C_{CSF} are the tracer activities in WM and CSF (which are assumed to be homogeneous, i.e. constant, in these tissue classes).

2.1.2. Region-based PVEc: background and implementation

An alternative method to the voxel-based PVEc was introduced by (Rousset et al., 1997, 1998a). This method attempts to recover the mean tracer signals within a set of non-overlapping regions-of-interest (ROI) representing different brain structures and tissue types, usually segmented in MRI (or CT) as a priori information.

Here, the true tracer uptake is assumed to be homogeneous within each ROI considered and spill-over effects between the different ROIs are estimated by convolving the binary ROI masks with the scanner PSF. To derive an estimate of the relative influence that the signal in a given ROI "A" exerts onto the measured signal in its neighboring ROI "B", the ROI mask "A" is convolved by the PSF (creating the regional spread function, *RSF*), and the probabilistically weighted sum of voxels overlapping the ROI "B" is calculated. This overlap is then divided by the total number of voxels in ROI "B". These estimates (or weights) form a so called geometric transfer matrix (GTM) with elements ω_{ij} describing the estimated spill-over effects between all pairs of brain regions:

$$\omega_{ij} = \frac{1}{\nu_j} \int_{ROI_j} RSF_i(r)\,dr$$

ω_{ij} represent the fraction from ROI_i that overlaps the ROI_j with volume υ_j and r is the space coordinate in the image space.

The observed regional intensity values (t_j) are considered to reflect a transformation of the true regional tracer concentrations (T_j) due to spill-over effects between regions with different intensity profiles. This transformation is estimated in the GTM, and thus the true tracer concentrations at each region (T_j) can be obtained by:

$$T_j = GTM^{-1} * t_j$$

2.2. PETPVE12 - partial volume effect correction toolbox

2.2.1. PVEc-MG module

Together with the subject's PET image, the main inputs for this module are the GM, WM and CSF tissue maps derived from segmenting the structural MRI scan. By default, these are defined in the toolbox as probabilistic maps generated by an adapted version of the segmentation algorithm included in the VBM8 toolbox (http://www.neuro.uni-jena.de/vbm/download/; see details below, Section 2.3.4), but the toolbox also accepts probabilistic maps derived from other segmentation algorithms (such as those inherent to SPM12). As an additional option, the tissue maps may also be defined as binary tissue maps, such as the "PVE-labeled images" generated by the VBM8 toolbox (detailed info can be found in the VBM8 documentation). Several choices exist for estimating the WM signal (C_{WM}) used in the PVEc-MG algorithm. The default approach is to estimate C_{WM} by measuring the average signal within a WM ROI derived from thresholding the WM tissue probability map of the normalization template, which is then propagated to native space by the inverse warping parameters identified through spatial normalization of the subject's MRI scan. However, other user-defined WM ROIs (e.g. the centrum semiovale) in native or normalized space may also be used. In order to minimize atlas propagation inaccuracies the default normalization approach uses the high-dimensional non-linear registration algorithm "DARTEL" (Ashburner, 2007; Klein et al., 2009; Martino et al., 2013) in combination with a DARTEL-compatible MNI space template provided by the VBM8 toolbox (the "IXI550_MNI152" template; see http://dbm.neuro.uni-jena.de/vbm8/VBM8-Manual.pdf for details). Alternatively, the C_{WM} value can also be estimated as the average activity within the subject's segmented WM map in native space, for which the intensity threshold applied to the probabilistic WM tissue map is set by the user. As a third option, the module also allows using the corrected WM signal obtained by the GTM method as the constant factor in the PVEc-MG algorithm; a method known as the "modified MG" approach (Rousset et al., 1998b).

For CSF, the default option is to estimate the signal analogously to the WM compartment, but, if justified by prior knowledge, the CSF signal can be set to zero (i.e. no tracer uptake) in this compartment (Erlandsson et al., 2012; Quarantelli et al., 2004).

2.2.2. PVEc-GTM module

For the PVEc-GTM, the series of continuous non-overlapping ROIs is usually obtained from an anatomical atlas defined on individual high spatial resolution MRI. By default, the toolbox defines neuroanatomical regional delimitations in MNI space according to those of the Desikan Killiany atlas (Desikan et al., 2006). However, given that the correction outcome of PVEc-GTM depends on the definition of the brain regions that are being considered in the algorithm (Edison et al., 2013), the toolbox provides the flexibility to let the user specify the preferred anatomical (or functional) cerebral parcellation atlas in template space (for an overview of some of the most widely used brain atlases in MNI space see e.g. http://www.lead-dbs.org/?page_id=1004; the PETPVE12 toolbox itself currently only includes the Desikan-Killiany atlas). In any case, the module propagates the template space parcellation atlas of choice to the individual MRI and then limits the ROIs to the segmented GM tissue, thresholded at 50% gray matter probability (Firbank et al., 2008; Rodrigue et al., 2012; Sun et al., 2007; Wong et al., 2010). Atlas propagation is based on inverse warping using the deformation fields obtained from spatial normalization of the subject's MRI scan (Ashburner, 2007).

Previous work has shown that a trustworthy PVEc on a region-basis should not be limited to correcting spill-over effects between different GM structures of interest, but must also consider spill-over effects from WM and extra-parenchymal background signal (Brendel et al., 2014; Thomas et al., 2011). This is especially important in the case of existing amyloid binding radiotracers, which usually exhibit high unspecific WM binding signal (Matsubara et al., 2016; Schmidt et al., 2015; Villemagne et al., 2012). Accordingly, a background region is automatically created by the GTM module before region-based correction is performed, and an additional option to define distinct WM regions (as opposed to the standard segmented WM tissue map) is provided.

2.2.3. Atlas-based quantification

As an additional utility, the toolbox offers a module with different options for the extraction of regional signals from the PET data. While regional signal extraction is inherent in the GTM method, this module may be used to extract regional signals from non-corrected PET data or the voxel-wise maps generated by the PVEc-GM module. The utility requires the specification of a parcellation atlas or a set of single ROIs, which can be defined either in an individual's native space or in a reference space template. In the latter case, an additional file has to be provided that describes the spatial mapping between native space and the reference template space.

2.3. Partial volume effects correction of AV45-PET data

In order to demonstrate the utility of the methods provided by the PETPVE12 toolbox, we assessed the effects of the two different PVEc methods on a large sample of AV45-PET scans provided by the Alzheimer's Disease Neuroimaging Initiative (ADNI).

2.3.1. Subjects

Analyses included AV45-PET and structural MRI data of 264 subjects enrolled in the ADNI-2 study (http://www.adni-info.org/), including 179 cognitively normal older individuals (CN) and 85 AD dementia patients. General inclusion criteria in the ADNI study are an age between 55 and 90 years, a modified Hachinski score≤4, education of at least 6 grade level, and stable treatment of at least 4 weeks in case of treatment with permitted medication (for full list see http://www.adni-info.org, Procedures Manual). Detailed description of the diagnosis-specific ADNI inclusion and exclusion criteria can be found at the ADNI website (http://www.adni.loni.usc.edu/methods/). Briefly, CN subjects have "Mini-Mental State Examination" (MMSE) (Cockrell and Folstein, 1988) scores between 24 and 30 (inclusive; MMSE test range 0–30), a "Clinical Dementia Rating" (CDR; test range 0–3) (Morris, 1993) score of 0, non-depressed, non-MCI, and non-demented. AD dementia patients have MMSE scores between 20 and 26 (inclusive), CDR scores of 0.5 or 1.0, and meet NINCDS/ADRDA criteria for probable AD (McKhann et al., 1984). Sample characteristics of the CN and AD groups included in this study are summarized in Table 1.

2.3.2. Imaging data acquisition

ADNI-2 MRI data were acquired on multiple 3 T MRI scanners using scanner-specific T1-weighted sagittal 3D MPRAGE sequences. In order to increase signal uniformity across the multicenter scanner platforms, original MPRAGE acquisitions in ADNI undergo standardized image pre-processing correction steps. AV45-PET data were

Table 1
Group demographics.

	CN subjects	AD patients
N	179	85
Age (years)	73.8 ± 6.4	75.6 ± 8.3
Gender (F/M)	91/88	36/49
Education	16.6 ± 2.5	15.7 ± 2.8*
MMSE	29.1 ± 1.2	22.9 ± 2*

AD: Alzheimer's disease; differences compared to cognitively normal control group (CN). Data are mean ± standard deviation; N: number of participants in each diagnostic group; F/M: female/male; MMSE: Mini Mental Status Examination.

* Statistically significant ($P < 0.05$).

acquired on multiple instruments of varying resolution and following different platform-specific acquisition protocols. Similar to the MRI data, PET data in ADNI undergo standardized image pre-processing correction steps aimed at increasing data uniformity across the multi-center acquisitions. All images were retrieved from the ADNI database server in the most fully pre-processed format (Advanced search: "AV45 Coreg, Avg, Std Img and Vox Siz, Uniform Resolution" for PET data; and: "MR_MT1, GradWarp, N3m" for MRI data). More detailed information on the different imaging protocols employed across ADNI sites and standardized image pre-processing steps for MRI and PET acquisitions can be found on the ADNI website (http://adni.loni.usc.edu/methods/).

2.3.3. MRI processing

The PETPVE12 toolbox includes the automated segmentation approach implemented in the VBM8 toolbox, which is described in detail elsewhere (Gaser, 2009). Briefly, segmentation is firstly obtained from the intensity distribution of the image. Separation into different tissue compartments (GM, WM and CSF) is based on an adaptive Maximum a Posterior (AMAP) approach (Rajapakse et al., 1997) with partial volume estimation (Tohka et al., 2004), and is further refined by applying an iterative hidden Markov random field model (Cuadra et al., 2005) to remove isolated voxels which are unlikely to belong to a determinate tissue type or are unable to be classified. Intensity values in the resulting maps represent a probability to belong to a pure tissue type (Gaser, 2009). The segmentation algorithm implemented in the toolbox has been modified to automatically create a brain mask, which may be used for skull-stripping before PET-MRI coregistration.

Due to the specific characteristics of our study population consisting of aged and demented subjects, segmented tissue compartments were high-dimensionally registered to an aging/AD-specific reference template instead of the toolbox's default MNI template (Grothe et al., 2013), which is intended to reduce a potential registration bias between AD patients and controls (Shen et al., 2012; Sun et al., 2007).

2.3.4. AV45-PET processing and quantification

AV45-PET data were coregistered to the structural MRI data and corrected for PVE using the voxel-wise PVEc-MG and the region-wise PVEc-GTM methods as described above. Study-specific settings included specification of an isotropic PSF of 8 mm (the effective image resolution of the ADNI AV45-PET data; toolbox default is 7 mm) and a brain parcellation based on the "Hammers" anatomical atlas (Hammers et al., 2003) for the PVEc-GTM module (Brendel et al., 2015) (atlas not included in the toolbox, but available upon request from: http://brain-development.org/brain-atlases/adult-brain-maximum-probability-map-hammers-mith-atlas-n30r83-in-mni-space/). The brain parcellation atlas in MNI space was matched to our study-specific aging/AD reference template using DARTEL registration. Global cortical standard uptake values (SUV) were calculated for each of the different processing approaches (non-corrected, PVEc-MG and PVEc-GTM corrected). For non-corrected and PVEc-GM data this was done by sampling the average signal within a neocortical composite mask in native space, created by inverse propagation of a reference space mask covering frontal, parietal, lateral temporal, insula, anterior and posterior cingulate cortices, and excluding those regions that are considered to be relatively preserved in AD (pre-, para- and post-central gyrus, medial temporal and occipital cortices) (Teipel et al., 2014). For the region-based PVEc-GTM method, global cortical SUVs were calculated by computing a volume-weighted average of the corrected values of corresponding neocortical regions as those used to create the composite mask. All global cortical SUVs were converted to standard uptake value ratios (SUVR) using the whole cerebellar signal in the individual raw PET images as the reference signal.

For voxel-based analyses, both non-corrected and PVEc-MG corrected AV45-PET images were spatially warped using the deformation fields derived from DARTEL registration of the coregistered MRI scans to the reference template. Warped images were smoothed with a Gaussian kernel of 8 mm.

2.3.5. Statistical analysis

2.3.5.1. Effect of PVEc on cortical AV45 standard uptake value ratios. For each of the two PVEc methods, the effect on global cortical SUVRs was assessed qualitatively using Bland-Altman plots, i.e. by plotting the difference between the corrected and non-corrected values against the mean of the two values. In addition, for each diagnostic group separately, the differences between PVEc and non-corrected SUVRs were assessed using paired t-tests.

2.3.5.2. Effect of PVEc on group differences in AV45 standard uptake value ratios. For each processing approach (non-corrected, PVEc-MG and PVEc-GTM), diagnostic group differences (AD vs CN) in global cortical SUVRs were assessed using two-sample t-tests of the group means. In addition, effect sizes of the group differences in global cortical SUVRs were assessed using standardized Cohen's d. Finally, the effect of PVEc on the accuracy of diagnostic group discrimination was assessed by computing Area Under the Curve (AUC) values derived from Receiver Operating Characteristic (ROC) analyses. 95% confidence intervals (CI) and significance of differences between AUC values derived from the different processing approaches were calculated using a bootstrap approach with 10,000 iterations implemented in the R-package "pROC" (Robin et al., 2011).

In addition to the analysis of commonly used global cortical SUVRs, we also assessed regional effects of PVEc on the voxel-level, which is a unique feature of the PVEc-MG approach. Thus, voxel-wise differences in AV45 SUVR between the CN and AD groups were assessed using 2-sample t-tests on non-corrected and PVEc-MG corrected AV45 PET images. Both statistical models included age and gender as covariates while proportional scaling the data to the whole cerebellum mean. Effects were assessed at a voxel-wise statistical threshold of $p < .05$, corrected for multiple comparisons using the family wise error rate.

3. Results

3.1. Sample characteristics

As summarized in Table 1, CN subjects tended to be younger than AD subjects (p=0.054) and had significantly more years of education (p=0.009). Gender distribution was comparable among groups (p=0.24). As expected, the AD group had significantly lower MMSE scores compared to the CN group ($p < 0.001$).

3.1.1. Effects of partial volume effects correction on global cortical AV45 SUVRs

Bland-Altman plots (Fig. 1) show that PVEc has a differential effect on SUVRs depending on the magnitude of the SUVR value: in the low to middle range of SUVRs both PVEc methods generally result in a decrease in SUVR, whereas at the high range of values both PVEc methods result in increased values. Most of the CN subjects (blue points) have SUVRs in the low range of the observed spectrum and PVEc generally further decreases these values. By contrast, most AD subjects (red points) have SUVRs in the high range of the spectrum and PVEc further increases most of these values.

Fig. 2 depicts bar plots of the mean SUVR values of the CN and AD groups derived from the different processing approaches (non-corrected, PVEc-MG, PVEc-GTM). In line with the observations in the Bland-Altman plots, both PVEc methods resulted in significantly decreased AV45 SUVR means for the CN group (PVEc-MG: −4.6%, p

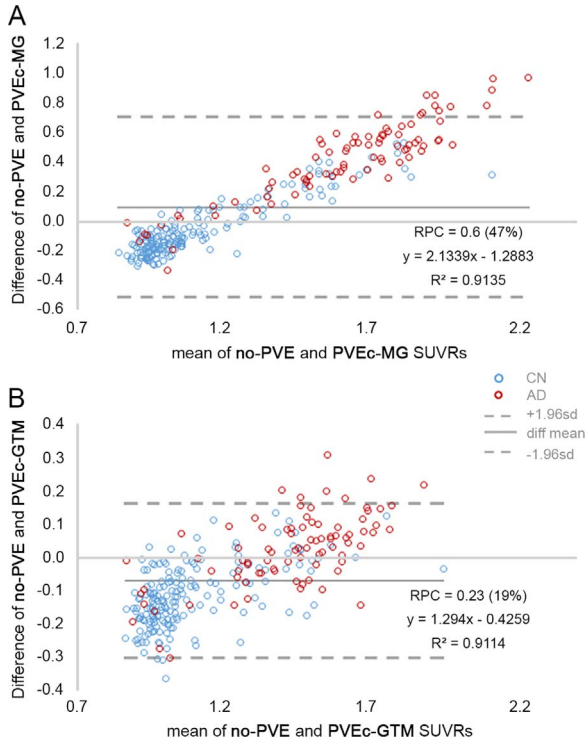

Fig. 1. Bland-Altman plot (difference plot) of global cortical SUVRs (AV45 cortical-composite-to-cerebellum) between no-PVEc and PVEc-MG (A) and no-PVEc and PVEc-GTM (B). x-axis is the average of the global cortical SUVRs from the two methods for each image, the y-axis is the difference in global cortical SUVRs. No-PVEc = non-corrected AV45-PET data, PVEc-MG = voxel-based partial volume effects correction, PVEc-GTM = region-based partial volume effects correction. AD = Alzheimer's disease, CN = cognitively normal controls. SUVR = standard uptake value ratios, RCP = reproducibility coefficient (% of mean values).

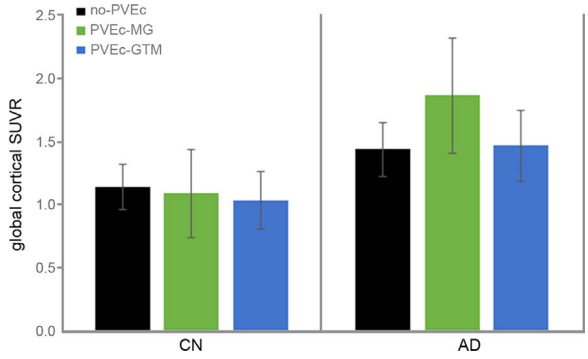

Fig. 2. Effect of PVEc on global cortical SUVR by diagnostic group. Bar plots represent group means of global cortical standard uptake value ratios (SUVR) derived from non-corrected (no-PVEc, black), voxel-based corrected (PVEc-MG, green) and region-based corrected (PVEc-GTM, blue) AV45-PET data. AD = Alzheimer's disease, CN = cognitively normal controls.

< 0.001; PVEc-GTM: −9.7%, p < 0.001) and increased AV45 SUVR means for the AD group (PVEc-MG: +29.7%, p < 0.001; PVEc-GTM: +1.9%, p=0.012).

3.2. Effects of partial volume effects correction on SUVR differences between patients and controls

Global cortical SUVR values were significantly different between the CN and AD groups for all processing approaches (Table 2). However, Cohen's d effect size estimates indicated increased group differences for both PVEc methods as compared to the non-corrected SUVR values. Similarly, both PVEc methods resulted in increased AUC values for the differentiation between CN and AD (Table 2 and Fig. 3). Increases in

Table 2
SUVR changes comparisons.

	non-corrected	PVEc-MG	PVEc-GTM
p val	< 0.001*	< 0.001*	< 0.001*
Standardized Cohen's d	1.55	2	1.75
AUC (95%-CI)	0.84 (0.78–0.90)	0.89 (0.84–0.93)**	0.86 (0.8–0.91)

Non-corrected: statistics based on global cortical AV45 SUVR values without Partial Volume Effects correction (PVEc); PVEc-MG: statistics based on global cortical AV45 SUVR values corrected using the voxel-based method; PVEc-GTM: statistics based on global cortical AV45 SUVR values corrected using the region-based method; p val: p-values for group differences (t-test); AUC (95%-CI): area under the curve and 95% confidence intervals.

* Statistically significant (p < 0.05) difference in global cortical AV45 SUVR compared to cognitively normal control group (CN).

** Statistically significant differences compared to AUC derived from non-corrected global cortical AV45 SUVR values.

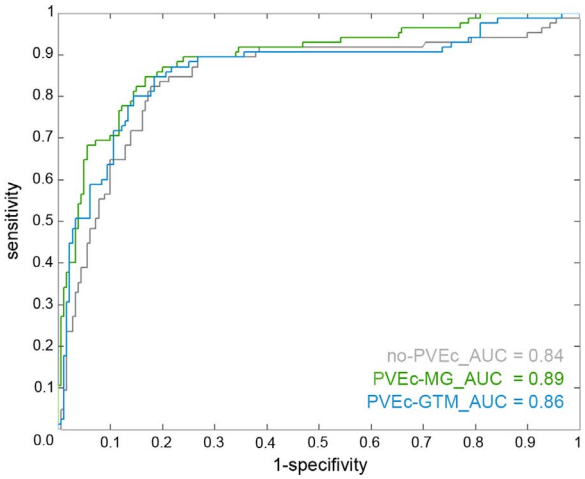

Fig. 3. Receiver-operating characteristic (ROC) curves for group discrimination between control (CN) and Alzheimer's disease (AD). non-corrected global cortical AV45 SUVR data (no-PVEc, black line), voxel-based partial volume effects correction (PVEc-MG, green line) and region-based partial volume effects correction (PVEc-GTM, blue line). AUC = area under the curve.

AUC values compared to the non-corrected approach were highly significant for PVEc-MG (p=0.0002) and trend-level significant for PVEc-GTM (p=0.09).

In voxel-wise analyses of regional AV45 SUVR group differences, highly significant SUVR increases in the AD group could be detected across wide parts of the cortex in both non-corrected and PVEc-MG data (Fig. 4). Direct comparison of the color-coded statistical maps shows higher T-values in the PVEc-MG data in several cortical regions known for high amyloid accumulation, such as the medial parietal and medial and lateral frontal cortices (Fig. 4).

4. Discussion

Quantification capability is generally considered a major advantage of PET amongst modalities for functional in vivo imaging. Consequently, considerable efforts have been made to improve absolute quantification (in kBq/ml) of the tracer distribution in PET. Methods for correction of physical effects associated with the formation of events such as photon attenuation and scatter have been implemented in the system software of PET scanners for routine use in everyday clinical patient care. The situation is different for effects related to limited spatial resolution of PET imaging, usually referred to as partial volume effects (Erlandsson et al., 2012; Kessler et al., 1984). Although PVE can be large and various PVEc methods have been developed (an excellent review is given in Erlandsson et al., 2012),

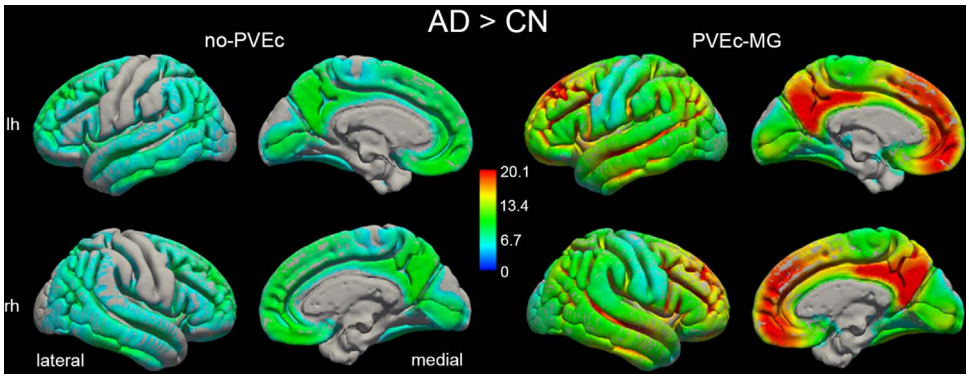

Fig. 4. Voxel-wise group differences before and after Partial volume effects correction. Statistical maps of group differences (thresholded at p(FWE) < 0.05) are represented at the same color-coded T-value scale to facilitate visual comparison. Increased T-statistics of group differences in the PVEc-MG data are particularly pronounced in the precuneus/posterior cingulate and medial frontal cortices. No-PVEc = non-corrected AV45-PET data, PVEc-MG = voxel-based partial volume effects correction. AD = Alzheimer's disease, CN = cognitively normal control. lh = left hemisphere, rh = right hemisphere.

PVEc is not yet widely used, either in whole-body PET or in brain PET. The latter might be explained by 'mixed' results of PVEc in FDG-PET of the brain. Reduction of cerebral glucose metabolism in neurodegenerative diseases is often accompanied by loss of gray matter, increasing the bias in recovered signal due to PVEs with surrounding low signal CSF and WM tissue. As a consequence, PVEs increase both magnitude and spatial extent of disease-related signal reductions in FDG-PET which often simplifies detection and differential diagnosis of neurodegenerative diseases (Ibanez et al., 1998; Meltzer et al., 1996; Samuraki et al., 2007). Eliminating these effects by PVEc can hamper the interpretation of brain FDG-PET in patients with suspected neurodegenerative disease. Possible PVEc-induced increases of statistical noise can further complicate the interpretation of PVE-corrected FDG-PET brain images.

In contrast to the metabolic decreases detected by FDG-PET, amyloid PET aims at detecting (or excluding) increased tracer retention in cortical gray matter. Thus, here PVEc is expected to increase (rather than decrease) the signal-to-background ratio, particularly in case of amyloid tracers with high nonspecific binding in adjacent white matter. Thus, here PVEc is expected to improve not only quantitative estimates of amyloid burden but also the potential to detect Alzheimer's disease. However, PVEc is not commonly applied in amyloid PET either. This may at least partly be due to the lack of PVEc options in the most widely used software packages for the analysis of brain PET images, such as the SPM software. SPM is a freely available, widely used, well documented open source tool kit, and therefore appears a suitable framework to support more widespread use of PVEc. The aim of the present work was to develop and validate an SPM toolbox for PVEc. The novel SPM PVEc toolbox, PETPVE12, features the 3-compartment method proposed by Müller-Gärtner and co-workers for voxel-based PVEc (PVEc-MG) (Muller-Gartner et al., 1992) and the geometric transfer matrix method (PVEc-GTM) (Rousset et al., 1997, 1998a) described by Rousset and colleagues for region-based PVEc in brain PET. Both methods use anatomical information (e.g. from individual structural MRI) to delineate GM in the brain and uniformity assumptions to limit amplification of noise and, most importantly, both methods are quite stable and very well validated. The user interface of PETPVE12 was designed to make the application of these two methods as flexible and as transparent as possible. The rationale for this was that (i) the results of PVEc strongly depend on each processing step and (ii) the optimal choice of processing steps and their parameter settings depends on the data to be analyzed. Thus, it is important to give the user the possibility to easily control settings for all processing steps.

As a first application we used the PETPVE12 toolbox for PVEc of amyloid-sensitive AV45-PET data of 85 AD patients and 179 CN subjects from the ADNI database. Major findings of this first application of the toolbox's PVEc methods were that (i) PETPVE12 performed adequately in all subjects, i.e. visual inspection of PVE-corrected images did not show obvious failures, (ii) applying the PVEc methods brought about a further decrease of global cortical SUVR for cases in the low to middle range of non-corrected SUVR and an increase of global cortical SUVR for cases in the upper range of non-corrected SUVR, which resulted in (iii) decreased global cortical SUVR in CN subjects and increased global cortical SUVR in AD patients, and (iv) increased effect size of the difference of global cortical SUVR between CN and AD subjects, that is, the increase of the difference in group mean overcompensated any possible increases in statistical noise. The latter indicates improved power of PVE-corrected AV45-PET images as a biomarker to support the diagnosis of AD (similar to previous findings by Rousset and co-workers suggesting improved power of PVE-corrected FDOPA-PET for detection of Parkinson's disease (Rousset et al., 2000)). The toolbox's PVEc methods need to be tested in longitudinal data, to establish if they can also improve the predictive accuracy of AV45-PET for MCI prognosis. Our analyses also demonstrated (for the first time) increased group differences in regional SUVR after PVEc on the voxel-level. While significant increases of cortical amyloid deposition in AD patients were detected across most cortical regions using both PVEc-MG corrected and non-corrected data, PVEc-MG resulted in up to 1.5-fold increased T-values for brain regions that are known to accumulate high levels of amyloid, such as anterior and posterior cingulate and precuneus. Increased sensitivity of PVE-corrected amyloid-PET may be particular relevant for the detection of subtle changes in amyloid signal, such as in the earliest stages of amyloidosis in the preclinical phase of AD or after short-term intervention effects.

The ROI-based findings of the present study are in good agreement with previous studies (Brendel et al., 2015; Rullmann et al., 2016; Su et al., 2016, 2015; Thomas et al., 2011). Brendel and colleagues, using the GTM-method for PVEc of ADNI AV45-PETs, also found global cortical SUVR to decrease in healthy subjects and to increase in AD subjects, resulting in improved discriminatory power of AV45-PET (Brendel et al., 2015). They also found PVEc to result in larger longitudinal increases of cortical AV45, that were most pronounced in amyloid-positive subjects (Brendel et al., 2015). Consistently, improved sensitivity to group differences and longitudinal changes was also reported by Su and co-workers for cortical C-11-PIB retention in autosomal dominant AD (Su et al., 2016). Rullmann and co-workers, using the modified PVEc-MG method on F-18-florbetaben PET in 3 different patient cohorts, found PVEc not only to increase Cohen's d effect size of the global cortical SUVR for the discrimination between AD patients and healthy controls, but also to improve the correlation between mesial temporal cortex SUVR and local amyloid plaque load according to histopathology (Rullmann et al., 2016). Thomas and co-

workers, using the modified PVEc-MG method in amyloid-PET with F-18-flutemetamol, found significantly increased effect size of the SUVR group difference between elderly healthy controls and AD patients in the frontal and the parietal lobe (Thomas et al., 2011). However, here, PVEc resulted in increased global cortical SUVR not only in the AD group but also in the group of elderly healthy controls, although the larger increase was seen in the AD group (Thomas et al., 2011). This is in contrast to reduced global cortical SUVR in the CN group in the present study and the report by Brendel et al. (2015). This difference might be explained as follows. The principal PVE in brain PET is the spill-over of counts between different brain regions with inherently differing tracer uptake, particularly between gray and white matter, as illustrated by the operational equation of the PVEc-MG (subsection 2.1.1 in the Methods; here we assume zero CSF tracer concentration for simplicity)

$$C_{obs}=(GM \otimes PSF)C_{GM}+ \quad (WM \otimes PSF)C_{WM}$$

In gray matter, spill-over counts can be seen as the net effect of spill-out of counts from gray matter and spill-in of counts from white matter

$$C_{GM,obs}=C_{GM}+\{\underbrace{(WM \otimes PSF)C_{WM}}_{\text{spill-in}}-\underbrace{[1-(GM \otimes PSF)]C_{GM}}_{\text{spill-out}}\}$$

The magnitude of the spill-out effect depends on the thickness of cortical gray matter, with greater spill-out for thinner cortex. Thus, spill-out not only depends on the localization in the brain (typically more pronounced in occipital than in frontal lobe), but it also increases with the amount of atrophy. Therefore, it is assumed to be higher in AD patients than in CN subjects. However, it is evident that the net effect of spill-out and spill-in is also influenced by the relationship of actual tracer binding between gray and white matter. In simplified terms: if actual tracer concentration is smaller in gray matter than in white matter (as expected in most CN subjects), spill-in of signal from WM into GM overcompensates loss of signal from GM due to spill out. In this case, PVEc is expected to result in decreased SUVR. The other way round: if actual tracer concentration is larger in gray than in white matter (as expected in most AD patients), the signal spill-out from GM is larger than the spill-in from WM and PVEc is expected to result in increased SUVR. Now, the relationship between tracer concentration in WM and GM depends not only on cortical amyloid load but also on the tracer used for PET imaging. C-11-PIB shows lower unspecific binding in WM than currently available F-18-labelled amyloid tracers, which may also differ with respect to unspecific white matter binding among themselves (Herholz and Ebmeier, 2011; Landau et al., 2014; Yousefi et al., 2015). Thus, different tracers, F-18-flutemetamol in the study by Thomas and colleagues versus AV45 in the present study, might contribute to differences in the relative effect of PVEc, particularly in CN subjects with low to middle range tracer concentration in gray matter, that is, below or close to tracer concentration in white matter. Further studies are needed to characterize potential differences in unspecific white matter binding among different F-18-labelled amyloid tracers and their possible impact on PVEc outcomes. The ROI used to characterize white matter uptake and the method to estimate true tracer concentration within this ROI (with or without PVEc, e.g. modified versus original PVEc-MG) may also contribute to some variability of results (Thomas et al., 2011). Furthermore, the SUVR is symmetric with respect to SUV variation in the region of interest and the reference region. Thus, different reference regions and different ways of estimating the SUV in the reference region (e.g. before versus after PVEc) also add to the variability of results. In addition, violation of the assumption of uniform tracer concentration within ROIs results in bias in PVE-corrected data, the magnitude of which varies between PVEc methods. There are further sources of variation in PVE-corrected results between studies, such as PET-MR co-registration, segmentation of gray matter (Frouin et al., 2002; Hogenauer et al., 2016) or variability of the error of spatial resolution assumed for the reconstructed PET images (as PVEc is sensitive to even small errors of the PSF) (Teo et al., 2007).

Considering the sensitivity of PVEc not only to the general method used, but also to each single preprocessing step involved in a given method as well as the parameter settings in these steps, we consider it an important advantage of the PETPVE12 toolbox to be very transparent with respect to the implemented routines and that it allows easy access to all parameter settings (rather than being a black box). As such, the PETPVE12 toolbox may provide a valuable tool for future research aimed at systematic analyses of the differential effects of differing PVEc methods, along with their respective processing options and parameter settings, on the outcomes of PVE-correction in amyloid-sensitive PET data as well as other PET modalities. In addition, given that SPM12 software is a very popular software tool for morphometric analyses of structural MRI data (Ashburner, 2009), the integration of PVEc processing options into SPM12 should markedly facilitate the study of the relationship between regional brain atrophy and PVE-corrected PET measures. This includes both methodical studies assessing the (probably) complex effects of regional brain atrophy on the magnitude of PVE correction (Rullmann et al., 2016), as well as clinical research studies investigating inter-modal association between MRI-derived estimates of regional brain atrophy and PET-based indices of regional pathology, such as hypometabolism or amyloid deposition in AD (Chetelat et al., 2009; La Joie et al., 2012; Oh et al., 2014; Teipel et al., 2016).

The toolbox provides the most widely used PVEc methods: PVEc-MG and PVEc-GTM. Theoretically, PVEc-GTM may provide more accurate results than voxel-based PVEc, given that it also accounts for possible spill-over effects between GM structures with differing tracer signal. However, it requires a priori specification of a specific cerebral parcellation scheme, and the assumption of homogenous tracer signal within the parcellated GM structures may not hold true for all ROIs. Future studies may assess possible advantages of using functional brain parcellations with assumedly more homogeneous intra-ROI tracer retention compared to the commonly used anatomical parcellation schemes. The PVEc-MG approach provides PVE-corrected PET images that can be used for explorative analyses using voxel-based testing. Thus, voxel-based and ROI-based PVEc usefully complement each other. In this context, it should be noted that the PVEc-MG is valid only for voxels in the gray matter target region and does not allow signal quantification of WM ROIs. A limitation of the PETPVE12 toolbox is that it only provides post-reconstruction PVEc methods. Reconstruction-based methods (Alessio and Kinahan, 2006; Rizzo et al., 2007) that account for the PSF during image reconstruction are expected to be more accurate than post-reconstruction methods.

In conclusion, the PETPVE12 toolbox facilitates access to PVEc either as stand-alone processing option or for integration into existing SPM processing pipelines for brain PET. We expect the toolbox to be particularly useful in brain amyloid binding PET by providing more accessible usage of well-validated PVEc methods that may improve quantitative estimates of amyloid burden, as well as the diagnostic and possibly also prognostic potential of AV45-PET in patients with suspected Alzheimer's disease.

Acknowledgments

Data collection and sharing for this project was funded by the Alzheimer's Disease Neuroimaging Initiative (ADNI) [(National Institutes of Health Grant U01 AG024904) and DOD ADNI (Department of Defense award number W81XWH-12-2-0012)]. The ADNI was launched in 2003 by the National Institute on Aging (NIA), the National Institute of Biomedical Imaging and Bioengineering (NIBIB), the Food and Drug Administration (FDA), private pharmaceutical companies and non-profit organizations, as a $60 million, 5-year public-private partnership. ADNI is funded by the National Institute on Aging, the National Institute of Biomedical Imaging and

Bioengineering, and through generous contributions from the following: Alzheimer's Association; Alzheimer's Drug Discovery Foundation; Araclon Biotech; BioClinica, Inc.; Biogen Idec Inc.; Bristol-Myers Squibb Company; CereSpir, Inc.; Eisai Inc.; Elan Pharmaceuticals, Inc.; Eli Lilly and Company; EuroImmun; F. Hoffmann-La Roche Ltd and its affiliated company Genentech, Inc.; Fujirebio; GE Healthcare; IXICO Ltd.; Janssen Alzheimer Immunotherapy Research & Development, LLC.; Johnson & Johnson Pharmaceutical Research & Development LLC.; Lumosity; Lundbeck; Merck & Co., Inc.; Meso Scale Diagnostics, LLC.; NeuroRx Research; Neurotrack Technologies; Novartis Pharmaceuticals Corporation; Pfizer Inc.; Piramal Imaging; Servier; Takeda Pharmaceutical Company; and Transition Therapeutics. The Canadian Institutes of Health Research is providing funds to support ADNI clinical sites in Canada. Private sector contributions are facilitated by the Foundation for the National Institutes of Health (www.fnih.org). The grantee organization is the Northern California Institute for Research and Education, and the study is coordinated by the Alzheimer's Disease Cooperative Study at the University of California, San Diego. ADNI data are disseminated by the Laboratory for Neuroimaging at the University of Southern California.

References

Alessio, A.M., Kinahan, P.E., 2006. Improved quantitation for PET/CT image reconstruction with system modeling and anatomical priors. Med. Phys. 33, 4095–4103.

Ashburner, J., 2007. A fast diffeomorphic image registration algorithm. NeuroImage 38, 95–113.

Ashburner, J., 2009. Computational anatomy with the SPM software. Magn. Reson. Imaging 27, 1163–1174.

Ashburner, J., Friston, K.J., 2000. Voxel-based morphometry–the methods. NeuroImage 11, 805–821.

Brendel, M., Delker, A., Rotzer, C., Boning, G., Carlsen, J., Cyran, C., Mille, E., Gildehaus, F.J., Cumming, P., Baumann, K., Steiner, H., Haass, C., Herms, J., Bartenstein, P., Rominger, A., 2014. Impact of partial volume effect correction on cerebral beta-amyloid imaging in APP-Swe mice using [(18)F]-florbetaben PET. NeuroImage 84, 843–853.

Brendel, M., Hogenauer, M., Delker, A., Sauerbeck, J., Bartenstein, P., Seibyl, J., Rominger, A., Alzheimer's Disease Neuroimaging, I., 2015. Improved longitudinal [(18)F]-AV45 amyloid PET by white matter reference and VOI-based partial volume effect correction. NeuroImage 108, 450–459.

Chetelat, G., Villain, N., Desgranges, B., Eustache, F., Baron, J.C., 2009. Posterior cingulate hypometabolism in early Alzheimer's disease: what is the contribution of local atrophy versus disconnection? Brain 132, e133, (author reply e134).

Clark, C.M., Schneider, J.A., Bedell, B.J., Beach, T.G., Bilker, W.B., Mintun, M.A., Pontecorvo, M.J., Hefti, F., Carpenter, A.P., Flitter, M.L., Krautkramer, M.J., Kung, H.F., Coleman, R.E., Doraiswamy, P.M., Fleisher, A.S., Sabbagh, M.N., Sadowsky, C.H., Reiman, E.P., Zehntner, S.P., Skovronsky, D.M., Group, A.A.S., 2011. Use of florbetapir-PET for imaging beta-amyloid pathology. JAMA 305, 275–283.

Cockrell, J.R., Folstein, M.F., 1988. Mini-Mental State Examination (MMSE). Psychopharmacol. Bull. 24, 689–692.

Cuadra, M.B., Cammoun, L., Butz, T., Cuisenaire, O., Thiran, J.P., 2005. Comparison and validation of tissue modelization and statistical classification methods in T1-weighted MR brain images. IEEE Trans. Med. Imaging 24, 1548–1565.

Desikan, R.S., Segonne, F., Fischl, B., Quinn, B.T., Dickerson, B.C., Blacker, D., Buckner, R.L., Dale, A.M., Maguire, R.P., Hyman, B.T., Albert, M.S., Killiany, R.J., 2006. An automated labeling system for subdividing the human cerebral cortex on MRI scans into gyral based regions of interest. NeuroImage 31, 968–980.

Edison, P., Carter, S.F., Rinne, J.O., Gelosa, G., Herholz, K., Nordberg, A., Brooks, D.J., Hinz, R., 2013. Comparison of MRI based and PET template based approaches in the quantitative analysis of amyloid imaging with PIB-PET. Neuroimage 70, 423–433.

Erlandsson, K., Buvat, I., Pretorius, P.H., Thomas, B.A., Hutton, B.F., 2012. A review of partial volume correction techniques for emission tomography and their applications in neurology, cardiology and oncology. Phys. Med. Biol. 57, R119–R159.

Firbank, M.J., Barber, R., Burton, E.J., O'Brien, J.T., 2008. Validation of a fully automated hippocampal segmentation method on patients with dementia. Human. Brain Mapp. 29, 1442–1449.

Frouin, V., Comtat, C., Reilhac, A., Gregoire, M.C., 2002. Correction of partial-volume effect for PET striatal imaging: fast implementation and study of robustness. J. Nucl. Med. 43, 1715–1726.

Gaser, C., 2009. Partial Volume Segmentation with Adaptive Maximum A Posteriori (MAP) Approach. Neuroimage 47, S39–S41.

Greve, D.N., Salat, D.H., Bowen, S.L., Izquierdo-Garcia, D., Schultz, A.P., Catana, C., Becker, J.A., Svarer, C., Knudsen, G.M., Sperling, R.A., Johnson, K.A., 2016. Different partial volume correction methods lead to different conclusions: an (18)F-FDG-PET study of aging. Neuroimage 132, 334–343.

Grothe, M., Heinsen, H., Teipel, S., 2013. Longitudinal measures of cholinergic forebrain atrophy in the transition from healthy aging to Alzheimer's disease. Neurobiol. Aging 34, 1210–1220.

Hammers, A., Allom, R., Koepp, M.J., Free, S.L., Myers, R., Lemieux, L., Mitchell, T.N., Brooks, D.J., Duncan, J.S., 2003. Three-dimensional maximum probability atlas of the human brain, with particular reference to the temporal lobe. Hum. Brain Mapp. 19, 224–247.

Herholz, K., Ebmeier, K., 2011. Clinical amyloid imaging in Alzheimer's disease. Lancet Neurol. 10, 667–670.

Hoffman, E.J., Huang, S.C., Phelps, M.E., 1979. Quantitation in positron emission computed tomography: 1. Effect of object size. J. Comput. Assist Tomogr. 3, 299–308.

Hogenauer, M., Brendel, M., Delker, A., Darr, S., Weiss, M., Bartenstein, P., Rominger, A., Alzheimer's Disease Neuroimaging, I., 2016. Impact of MRI-based Segmentation Artifacts on Amyloid- and FDG-PET Quantitation. Curr. Alzheimer Res. 13, 597–607.

Ibanez, V., Pietrini, P., Alexander, G.E., Furey, M.L., Teichberg, D., Rajapakse, J.C., Rapoport, S.I., Schapiro, M.B., Horwitz, B., 1998. Regional glucose metabolic abnormalities are not the result of atrophy in Alzheimer's disease. Neurology 50, 1585–1593.

Kessler, R.M., Ellis, J.R., Jr., Eden, M., 1984. Analysis of emission tomographic scan data: limitations imposed by resolution and background. J Comput. Assist Tomogr. 8, 514–522.

Klein, A., Andersson, J., Ardekani, B.A., Ashburner, J., Avants, B., Chiang, M.C., Christensen, G.E., Collins, D.L., Gee, J., Hellier, P., Song, J.H., Jenkinson, M., Lepage, C., Rueckert, D., Thompson, P., Vercauteren, T., Woods, R.P., Mann, J.J., Parsey, R.V., 2009. Evaluation of 14 nonlinear deformation algorithms applied to human brain MRI registration. Neuroimage 46, 786–802.

La Joie, R., Perrotin, A., Barre, L., Hommet, C., Mezenge, F., Ibazizene, M., Camus, V., Abbas, A., Landeau, B., Guilloteau, D., de La Sayette, V., Eustache, F., Desgranges, B., Chetelat, G., 2012. Region-specific hierarchy between atrophy, hypometabolism, and beta-amyloid (Abeta) load in Alzheimer's disease dementia. J. Neurosci. 32, 16265–16273.

Landau, S.M., Thomas, B.A., Thurfjell, L., Schmidt, M., Margolin, R., Mintun, M., Pontecorvo, M., Baker, S.L., Jagust, W.J., Alzheimer's Disease Neuroimaging, I., 2014. Amyloid PET imaging in Alzheimer's disease: a comparison of three radiotracers. Eur. J. Nucl. Med. Mol. Imaging 41, 1398–1407.

Martino, M.E., de Villoria, J.G., Lacalle-Aurioles, M., Olazaran, J., Cruz, I., Navarro, E., Garcia-Vazquez, V., Carreras, J.L., Desco, M., 2013. Comparison of different methods of spatial normalization of FDG-PET brain images in the voxel-wise analysis of MCI patients and controls. Ann. Nucl. Med. 27, 600–609.

Matsubara, K., Ibaraki, M., Shimada, H., Ikoma, Y., Suhara, T., Kinoshita, T., Itco, H., 2016. Impact of spillover from white matter by partial volume effect on quantification of amyloid deposition with [11C]PiB PET. Neuroimage 143, 316–324.

McKhann, G., Drachman, D., Folstein, M., Katzman, R., Price, D., Stadlan, E.M., 1984. Clinical diagnosis of Alzheimer's disease: report of the NINCDS-ADRDA Work Group under the auspices of Department of Health and Human Services Task Force on Alzheimer's Disease. Neurology 34, 939–944.

Meltzer, C.C., Zubieta, J.K., Brandt, J., Tune, L.E., Mayberg, H.S., Frost, J.J., 1996. Regional hypometabolism in Alzheimer's disease as measured by positron emission tomography after correction for effects of partial volume averaging. Neurology 47, 454–461.

Morris, J.C., 1993. The Clinical Dementia Rating (CDR): current version and scoring rules. Neurology 43, 2412–2414.

Muller-Gartner, H.W., Links, J.M., Prince, J.L., Bryan, R.N., McVeigh, E., Leal, J.P., Davatzikos, C., Frost, J.J., 1992. Measurement of radiotracer concentration in brain gray matter using positron emission tomography: mri-based correction for partial volume effects. J. Cereb. Blood Flow. Metab. 12, 571–583.

Oh, H., Habeck, C., Madison, C., Jagust, W., 2014. Covarying alterations in Abeta deposition, glucose metabolism, and gray matter volume in cognitively normal elderly. Hum. Brain Mapp. 35, 297–308.

Quarantelli, M., Berkouk, K., Prinster, A., Landeau, B., Svarer, C., Balkay, L., Alfano, B., Brunetti, A., Baron, J.C., Salvatore, M., 2004. Integrated software for the analysis of brain PET/SPECT studies with partial-volume-effect correction. J. Nucl. Med. 45, 192–201.

Rajapakse, J.C., Giedd, J.N., Rapoport, J.L., 1997. Statistical approach to segmentation of single-channel cerebral MR images. IEEE Trans. Med. Imaging 16, 176–186.

Rizzo, G., Castiglioni, I., Russo, G., Tana, M.G., Dell'Acqua, F., Gilardi, M.C., Fazio, F., Cerutti, S., 2007. Using deconvolution to improve PET spatial resolution in OSEM iterative reconstruction. Methods Inf. Med. 46, 231–235.

Robin, X., Turck, N., Hainard, A., Tiberti, N., Lisacek, F., Sanchez, J.C., Muller, M., 2011. pROC: an open-source package for R and S+ to analyze and compare ROC curves. BMC Bioinforma. 12, 77.

Rodrigue, K.M., Kennedy, K.M., Devous, M.D., Sr., Rieck, J.R., Hebrank, A.C., Diaz-Arrastia, R., Mathews, D., Park, D.C., 2012. beta-Amyloid burden in healthy aging: regional distribution and cognitive consequences. Neurology 78, 387–395.

Rousset, O., Ma, Y., Evans, A.C., 1997. ROI- versus tissue-based partial-volume correction [abstract]. Neuroimage 5, B13.

Rousset, O.G., Deep, P., Kuwabara, H., Evans, A.C., Gjedde, A.H., Cumming, P., 2000. Effect of partial volume correction on estimates of the influx and cerebral metabolism of 6-[(18)F]fluoro-L-dopa studied with PET in normal control and Parkinson's disease subjects. Synapse 37, 81–89.

Rousset, O.G., Ma, Y., Evans, A.C., 1998a. Correction for partial volume effects in PET: principle and validation. J. Nucl. Med. 39, 904–911.

Rousset, O.G., Ma, Y., Wong, D.F., Evans, A.C., 1998b. Pixel- versus region-based partial volume correction in PET. In: Carson, R.E., Herscovitch, P., Daube-Witherspoon, M.E. (Eds.), Quantitative Functional Brain Imaging with Positron Emission Tomography. Elsevier, Academic Press, San Diego, CA, 67–75.

Rullmann, M., Dukart, J., Hoffmann, K.T., Luthardt, J., Tiepolt, S., Patt, M., Gertz, H.J., Schroeter, M.L., Seibyl, J., Schulz-Schaeffer, W.J., Sabri, O., Barthel, H., 2016. Partial-volume effect correction improves quantitative analysis of 18F-Florbetaben beta-Amyloid PET scans. J. Nucl. Med. 57, 198–203.

Samuraki, M., Matsunari, I., Chen, W.P., Yajima, K., Yanase, D., Fujikawa, A., Takeda, N., Nishimura, S., Matsuda, H., Yamada, M., 2007. Partial volume effect-corrected FDG PET and grey matter volume loss in patients with mild Alzheimer's disease. Eur. J. Nucl. Med. Mol. Imaging 34, 1658–1669.

Schmidt, M.E., Chiao, P., Klein, G., Matthews, D., Thurfjell, L., Cole, P.E., Margolin, R., Landau, S., Foster, N.L., Mason, N.S., De Santi, S., Suhy, J., Koeppe, R.A., Jagust, W., Alzheimer's Disease Neuroimaging, I., 2015. The influence of biological and technical factors on quantitative analysis of amyloid PET: points to consider and recommendations for controlling variability in longitudinal data. Alzheimers Dement 11, 1050–1068.

Shen, Q., Zhao, W., Loewenstein, D.A., Potter, E., Greig, M.T., Raj, A., Barker, W., Potter, H., Duara, R., 2012. Comparing new templates and atlas-based segmentations in the volumetric analysis of brain magnetic resonance images for diagnosing Alzheimer's disease. Alzheimers Dement 8, 399–406.

Soret, M., Bacharach, S.L., Buvat, I., 2007. Partial-volume effect in PET tumor imaging. J. Nucl. Med. 48, 932–945.

Su, Y., Blazey, T.M., Owen, C.J., Christensen, J.J., Friedrichsen, K., Joseph-Mathurin, N., Wang, Q., Hornbeck, R.C., Ances, B.M., Snyder, A.Z., Cash, L.A., Koeppe, R.A., Klunk, W.E., Galasko, D., Brickman, A.M., McDade, E., Ringman, J.M., Thompson, P.M., Saykin, A.J., Ghetti, B., Sperling, R.A., Johnson, K.A., Salloway, S.P., Schofield, P.R., Masters, C.L., Villemagne, V.L., Fox, N.C., Forster, S., Chen, K., Reiman, E.M., Xiong, C., Marcus, D.S., Weiner, M.W., Morris, J.C., Bateman, R.J., Benzinger, T.L., Dominantly Inherited Alzheimer, N., 2016. Quantitative amyloid imaging in autosomal dominant Alzheimer's disease: results from the DIAN study group. PLoS One 11, e0152082.

Su, Y., Blazey, T.M., Snyder, A.Z., Raichle, M.E., Marcus, D.S., Ances, B.M., Bateman, R.J., Cairns, N.J., Aldea, P., Cash, L., Christensen, J.J., Friedrichsen, K., Hornbeck, R.C., Farrar, A.M., Owen, C.J., Mayeux, R., Brickman, A.M., Klunk, W., Price, J.C., Thompson, P.M., Ghetti, B., Saykin, A.J., Sperling, R.A., Johnson, K.A., Schofield, P.R., Buckles, V., Morris, J.C., Benzinger, T.L., Dominantly Inherited Alzheimer, N., 2015. Partial volume correction in quantitative amyloid imaging. Neuroimage 107, 55–64.

Sun, F.T., Schriber, R.A., Greenia, J.M., He, J., Gitcho, A., Jagust, W.J., 2007. Automated template-based PET region of interest analyses in the aging brain. Neuroimage 34, 608–617.

Teipel, S., Grothe, M.J., Alzheimer s Disease Neuroimaging, I., 2016. Does posterior cingulate hypometabolism result from disconnection or local pathology across preclinical and clinical stages of Alzheimer's disease? Eur. J. Nucl. Med. Mol. Imaging 43, 526–536.

Teipel, S., Heinsen, H., Amaro, E., Jr., Grinberg, L.T., Krause, B., Grothe, M., Alzheimer's Disease Neuroimaging, I., 2014. Cholinergic basal forebrain atrophy predicts amyloid burden in Alzheimer's disease. Neurobiol. Aging 35, 482–491.

Teo, B.K., Seo, Y., Bacharach, S.L., Carrasquillo, J.A., Libutti, S.K., Shukla, H., Hasegawa, B.H., Hawkins, R.A., Franc, B.L., 2007. Partial-volume correction in PET: validation of an iterative postreconstruction method with phantom and patient data. J. Nucl. Med 48, 802–810.

Thomas, B.A., Erlandsson, K., Modat, M., Thurfjell, L., Vandenberghe, R., Ourselin, S., Hutton, B.F., 2011. The importance of appropriate partial volume correction for PET quantification in Alzheimer's disease. Eur. J. Nucl. Med. Mol. Imaging 38, 1104–1119.

Tohka, J., Zijdenbos, A., Evans, A., 2004. Fast and robust parameter estimation for statistical partial volume models in brain MRI. Neuroimage 23, 84–97.

Videen, T.O., Perlmutter, J.S., Mintun, M.A., Raichle, M.E., 1988. Regional correction of positron emission tomography data for the effects of cerebral atrophy. J. Cereb. Blood Flow. Metab. 8, 662–670.

Villemagne, V.L., Klunk, W.E., Mathis, C.A., Rowe, C.C., Brooks, D.J., Hyman, B.T., Ikonomovic, M.D., Ishii, K., Jack, C.R., Jagust, W.J., Johnson, K.A., Koeppe, R.A., Lowe, V.J., Masters, C.L., Montine, T.J., Morris, J.C., Nordberg, A., Petersen, R.C., Reiman, E.M., Selkoe, D.J., Sperling, R.A., Van Laere, K., Weiner, M.W., Drzezga, A., 2012. Abeta Imaging: feasible, pertinent, and vital to progress in Alzheimer's disease. Eur. J. Nucl. Med. Mol. Imaging 39, 209–219.

Wong, D.F., Rosenberg, P.B., Zhou, Y., Kumar, A., Raymont, V., Ravert, H.T., Dannals, R.F., Nandi, A., Brasic, J.R., Ye, W., Hilton, J., Lyketsos, C., Kung, H.F., Joshi, A.D., Skovronsky, D.M., Pontecorvo, M.J., 2010. In vivo imaging of amyloid deposition in Alzheimer disease using the radioligand 18F-AV-45 (florbetapir [corrected] F 18). J. Nucl. Med. 51, 913–920.

Yousefi, B.H., von Reutern, B., Scherubl, D., Manook, A., Schwaiger, M., Grimmer, T., Henriksen, G., Forster, S., Drzezga, A., Wester, H.J., 2015. FIBT versus florbetaben and PiB: a preclinical comparison study with amyloid-PET in transgenic mice. EJNMMI Res. 5, 20.